Supporting Information

Suppression of Interfacial Water Layer with Solid Contact by an Ultrathin Water Repellent and Zn^{2+} Selective Layer for Ah-Level Zinc Metal Battery

Ziwei Xu[1], Junpeng Li[1], Yifan Fu[1], Junjie Ba[1], Fengxue Duan[1], Yingjin Wei[1], Chunzhong Wang*[1], Kangning Zhao*[2], and Yizhan Wang*[1]

1. Key Laboratory of Physics and Technology for Advanced Batteries (Ministry of Education), State Key Laboratory of Superhard Materials, College of Physics, Jilin University, Changchun, 130012, China. 2. School of Physical Sciences, Great Bay University, Dongguan, 523000, China.

*Correspondence: wangyizhan@jlu.edu.cn; vicyel@gbu.edu.cn; wcz@jlu.edu.cn

Experimental section

Material preparation

Synthesis of FeHCF/Zn Nanomembrane: 2 mL of a 0.05 M aqueous solution of potassium ferricyanide ($K_3Fe(CN)_6$) was added into a Petri dish with a diameter of 8.5 cm, followed by the addition of 20 mL of deionized water to ensure uniform mixing. Subsequently, 20 μL of dimethyldioctadecylammonium bromide (DODA) solution (1.8 mM in chloroform) was carefully dispersed onto the liquid surface and left undisturbed for 5 minutes to form a monolayer at the air–water interface. After that, 2 mL of a 0.025 M aqueous solution of ferric chloride ($FeCl_3$) was added dropwise into the solution. The mixture was allowed to react at room temperature for 20 hours, resulting in the formation of a FeHCF nanomembrane with a thickness of 16.9 nm at the air–water interface. The nanomembrane was then transferred onto a bare Zn foil substrate (6 × 6 cm^2) by slowly lifting the vertically placed substrate at the interface. Finally, the FeHCF/Zn foil was dried at 60 °C for 0.5 hours before use.

Synthesis of Large-Area FeHCF Nanomembrane: In a square container measuring 30 cm × 120 cm, 2000 mL of deionized water was added, followed by 200 mL of a 50 mM potassium ferricyanide solution. After ensuring uniform diffusion, 800 μL of DODA solution (1.8 mM in chloroform) was carefully dropped onto the air–water interface to form a monolayer. Subsequently, 200 mL of a 25 mM ferric chloride solution was injected below the liquid surface using a syringe. The reaction was allowed to proceed at room temperature for 20 hours, resulting in the formation of a FeHCF nanomembrane at the air–water interface.

Material characterization

X-ray photoelectron spectroscopy (XPS) was performed using a Thermo Scientific NEXSA system with a Mg Kα light source. During the fitting of the Fe 2p XPS signals, the constraints on the peak area ratio between Fe 2p 1/2 and Fe 2p 3/2 were set at 0.5. X-ray diffraction (XRD) patterns were recorded on a Bruker D8 Advance diffractometer with Cu Kα radiation. Atomic force microscopy (AFM) images were obtained using a Bruker Dimension FastScan system. Contact angle measurements were conducted at 25 °C using a water droplet shape analysis system with a droplet volume of 3 μL. In situ observation of

dendrite growth was performed using an Aosvi Optical Microscope (M330-HK830). Raman spectra were acquired using a Horiba LabRAM HR Evolution spectrometer with a 633 nm excitation source. Fourier-transform infrared (FT-IR) spectra were measured on a Bruker Vertex 80 V spectrometer. Scanning electron microscopy (SEM) images and energy-dispersive X-ray (EDX) spectroscopy were carried out on a Hitachi Regulus8100 microscope to characterize the surface morphology and elemental distribution. In situ pH measurements were conducted using a Mettler Toledo pH meter (AG30281915). Transmission electron microscopy (TEM) images were obtained using a JEOL JEM-2100F microscope operating at 200 kV. H-type cell diffusion experiment was performed with a hydrophilic polypropylene (PP) separator provided by Guangdong Candle New Energy Technology Co., Ltd. Its detailed physical properties are as follows: thickness 40 μm, areal density 21.3 g m^{-2}, porosity 41.20%, puncture strength 702.3 g, tensile strength 1674 kgf cm^{-2}, and heat shrinkage 0.50%.

Fabrication of cells

Symmetric Cells: Symmetric cells were assembled using two identical electrodes, either FeHCF/Zn or bare Zn, with a diameter of 1 cm. Glass fiber and 2 M aqueous $ZnSO_4$ solution were used as the separator and electrolyte, respectively.

Asymmetric Cells: Asymmetric cells were constructed using two different electrodes: the negative electrode was either FeHCF/Zn or bare Zn, and the positive electrode was FeHCF/Cu, bare Cu, FeHCF/Ti, or bare Ti. Glass fiber and 2 M aqueous $ZnSO_4$ solution were used as the separator and electrolyte, respectively.

Full Cells: In the full cells, the negative electrode was either FeHCF/Zn or bare Zn, and the positive electrode was either a CNT/MnO_2 composite or iodine-based electrode. For the preparation of the CNT/MnO_2 cathode, the active material, conductive carbon black (Super P), and polyvinylidene fluoride (PVDF) were mixed in a mass ratio of 7:2:1. The mixture was ground in n-methylpyrrolidone (NMP) for 20 minutes to form a uniform slurry. The slurry was then coated onto a titanium foil using a doctor blade and dried in a vacuum oven at 60 °C for 24 hours. The mass loading of the CNT/MnO_2 cathode was approximately 1 mg cm^{-2}. For the preparation of the iodine cathode, activated carbon, conductive carbon black (Super P), and polytetrafluoroethylene (PTFE) were mixed in a

mass ratio of 7:2:1. The mixture was dispersed in ethanol and ground into a dough-like consistency. The mixture was then rolled onto a titanium mesh and dried in a vacuum oven at 60 °C for 24 hours. An ethanol solution of iodine (1 g I_2 in 10 mL anhydrous ethanol) was added dropwise onto the activated carbon substrate using a pipette. The mass loading of the iodine cathode was typically 5–7 mg cm^{-2}.

Zn-Anode Free Full Cell: Activated carbon (AC), carbon nanotubes (CNTs), and a PTFE solution were mixed in an 8:1:1 mass ratio in ethanol and ground until a homogenous, rubber-like paste was obtained. This paste was uniformly coated onto a titanium mesh to prepare a cathodic substrate with an AC loading of approximately 15 mg cm^{-2}. Iodine (I_2) was dissolved in ethanol and drop-cast onto the AC substrate until a total of about 16 mg of I_2 was loaded. A full cell was then assembled by pairing a 10 μm-thick zinc foil (anode) with the I_2-loaded cathode (containing ~16 mg of active I_2), separated by a glass fiber membrane. The cell was infiltrated with 80 μL of 2 M $ZnSO_4$ electrolyte. For initial electrochemical testing, the cell was galvanostatically discharged and charged for five cycles at a constant current of 8 mA and then fully discharged. Subsequently, the cell was disassembled, and the cathode was recovered. A new full cell was constructed using the same cathode but replacing the Zn foil with a 10 μm-thick copper foil as the negative electrode. The same separator and electrolyte conditions were maintained. This second full cell was then galvanostatically cycled at 8 mA under a charge–discharge protocol.

Ah-level Full Cell: For high-loading electrodes, AC, CNTs, and PTFE solution were again mixed at an 8:1:1 mass ratio in ethanol and ground into a paste. This paste was coated on both sides of a 6 cm × 6 cm titanium mesh, achieving an AC loading of ~30 mg cm^{-2}. The coated mesh was dried at 60°C for 24 h. I_2 was then dissolved in ethanol and drop-cast onto the dried substrate until a total I_2 loading of 2 g per electrode was reached. The I_2-loaded electrodes were dried at room temperature for 24 h. Three such I_2-loaded cathodes and four 6 cm × 6 cm zinc foils (50 μm thick) were prepared. These were stacked in series to form a six-cell assembly: one Zn foil at the bottom, followed by an I_2-loaded cathode, then another Zn foil, and so forth. Each electrode pair was separated by a glass fiber membrane, and 2 M $ZnSO_4$ electrolyte was introduced to each cell. This configuration created a high-loading, multi-cell system to investigate performance under practical conditions.

Electrochemical Tests:

All galvanostatic charge/discharge and cycling tests were conducted on a LANHE CT3002AU battery test system. Electrochemical impedance spectroscopy (EIS) was performed using a DH7003 electrochemical workstation (Jiangsu Donghua Analytical Instrument Co., Ltd.) over a frequency range of 10^{-1} to 10^{5} Hz. Cyclic voltammetry (CV) measurements were carried out on the DH7003 workstation within voltage ranges of 0.8–1.8 V or 0.4–2.0 V at a scan rate of 0.1 mV s^{-1}. Chronoamperometry (CA) tests at a fixed overpotential of −150 mV was conducted using FeHCF/Zn and bare Zn symmetric cells to evaluate time-dependent current responses. Linear sweep voltammetry (LSV) was performed on FeHCF/Ti||Zn and bare Ti||Zn asymmetric cells. Corrosion tests were conducted in a three-electrode configuration with FeHCF/Zn (or bare Zn) as the working electrode, Ag/AgCl as the reference electrode, and applying 0–1 V at a step of 50 mV s^{-1}. Ionic conductivity tests were carried out for FeHCF/Zn and bare Zn symmetric cells over a frequency range of 10^{-1}–10^{-5} Hz.

To measure ionic conductivity, we employed SS||SS symmetric cells in a standard 2032-type coin-cell configuration. Each stainless-steel electrode has a diameter of 10 mm. The separator was a 200 μm thick glass-fiber membrane (Whatman GF/B), which also defines the interelectrode distance. The electrolyte was 2 M $ZnSO_4$. During assembly, no extra pressure was applied beyond the spring pressure inherent to the coin-cell crimping process, and care was taken to minimize compression-induced variation of the separator thickness. We performed electrochemical impedance spectroscopy (EIS) on the fully assembled SS||SS symmetric cells in the frequency range of 100 kHz to 1 Hz with an amplitude of 10 mV. The ionic conductivity can be obtained from Rs by fitting the following equation:

$$\kappa = L/(Rs*S)$$

where κ is the ionic conductivity, L is the Zn^{2+} diffusion distance. Rs and S are the electrolyte resistance and electrode surface, respectively.

To measure the transference number, we employed Zn||Zn symmetric cells in a standard 2032-type coin-cell configuration. Each Zn electrode was a 200 μm thick zinc foil

with a diameter of 10 mm. The separator was a 200 μm thick glass-fiber membrane (Whatman GF/B). The electrolyte was 2 M $ZnSO_4$. A constant polarization voltage (ΔV = 10 mV) was applied, and we recorded the initial current (I_0) and the steady-state current (I_s). EIS was measured before and after polarization to determine the initial and final resistances (R_0, Rs). Equation (1) was used to calculate t_{Zn}:

$$t_{zn} = \frac{I_s(\Delta V - I_o R_o)}{I_o(\Delta V - I_s R_s)}$$

where ΔV is the applied constant polarization voltage (10 mV), I_0 and R_0 are the initial current and resistance, respectively, and I_s and R_s are the steady-state current and resistance, respectively. The electrochemical impedance spectroscopy was tested using a DH7003 electrochemical testing unit with an amplitude of 10 mV ranging from 100 kHz to 0.01 Hz

Electric field calculations:

We employed finite element analysis using COMSOL Multiphysics® software to simulate the two-dimensional electrostatic field distribution during zinc deposition. The model geometry consisted of a 12 μm × 6 μm rectangular simulation domain, comprising a zinc electrode layer (1 μm thickness) and a zinc sulfate electrolyte layer (5 μm thickness). Multiple elliptical protrusions (major axis: 1 μm; minor axis: 0.4 μm; spacing: 4 μm) were incorporated to realistically mimic the polished zinc anode surface morphology. A conformal FeHCF nanomembrane (20 nm thickness) was introduced on top of these protrusions to simulate the protective interface. The relative dielectric constant of the FeHCF nanomembrane was set to 3.2, which was in line with reported values for Prussian Blue. An applied potential of 0.07 V was imposed between the electrolyte and the zinc electrode. The governing equations for the electrostatic field are as follows:

$$E = -\nabla V$$

$$\nabla \cdot (\varepsilon_0 \varepsilon_r E) = \rho_v$$

where, E, V, ε_0, ε_r and ρ_v represent the electric potential, the electrostatic field, the permittivity of free space, the relative permittivity and the space charge density respectively. The constitutive relationship of linear dielectric materials is assumed to be:

$$D = \varepsilon_0 \varepsilon_r E$$

where D represents the electric displacement field.

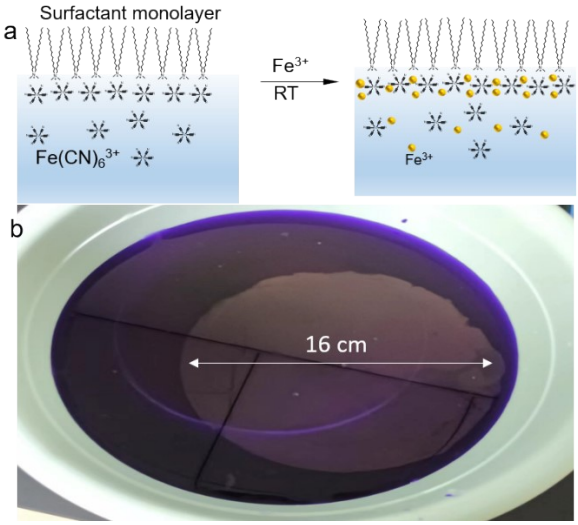

Figure S1. a, The schematic diagram of the synthesis of FeHCF nanomembrane. **b**, Photograph of the lifted free-floating FeHCF nanomembrane at air-water interface (Dye molecules were added into the aqueous solution to make nanomembrane more visible).

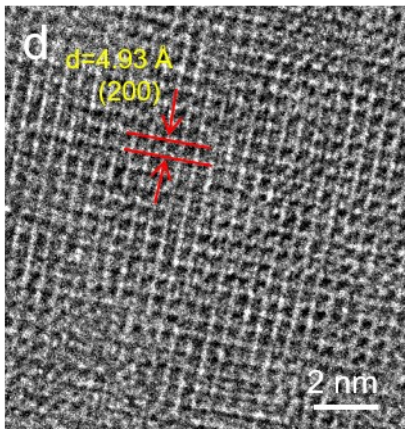

Figure S2. High-resolution TEM image of the FeHCF nanomembrane.

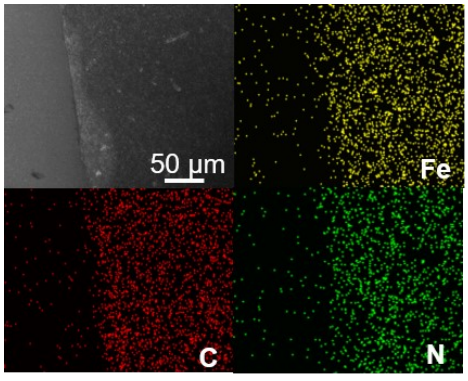

Figure S3. SEM EDS element mappings of Fe, N, and C.

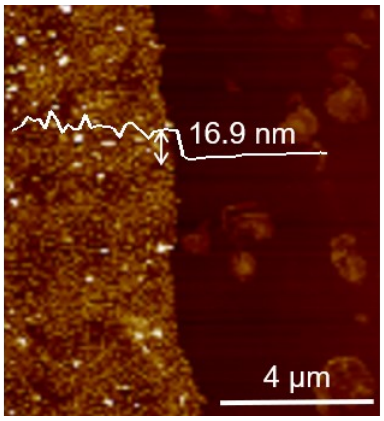

Figure S4. AFM measurement of the FeHCF/Zn.

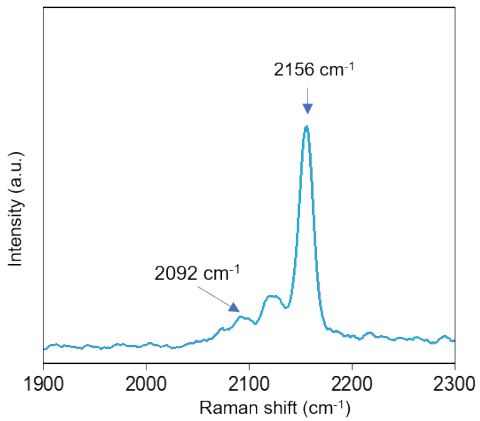

Figure S5. Raman spectrum of FeHCF nanomembrane on silica wafer.

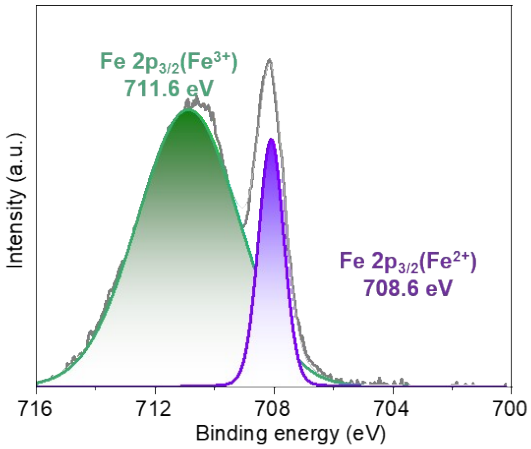

Figure S6. Fe 2p3/2 XPS of FeHCF nanomembrane on silica wafer.

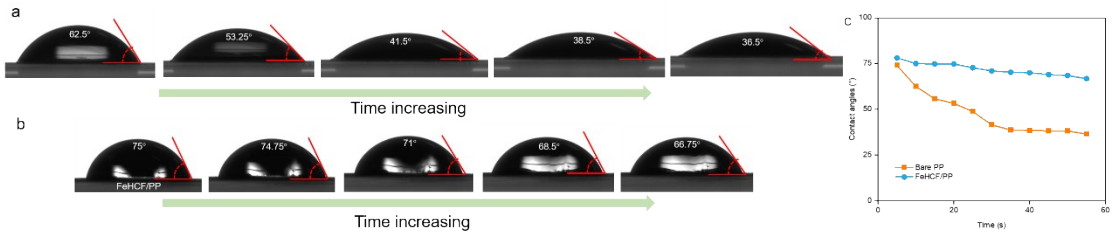

Figure S7. The change of contact angles of a) bare PP and b) FeHCF/PP within 60 seconds. c. the plots of contact angles vs time.

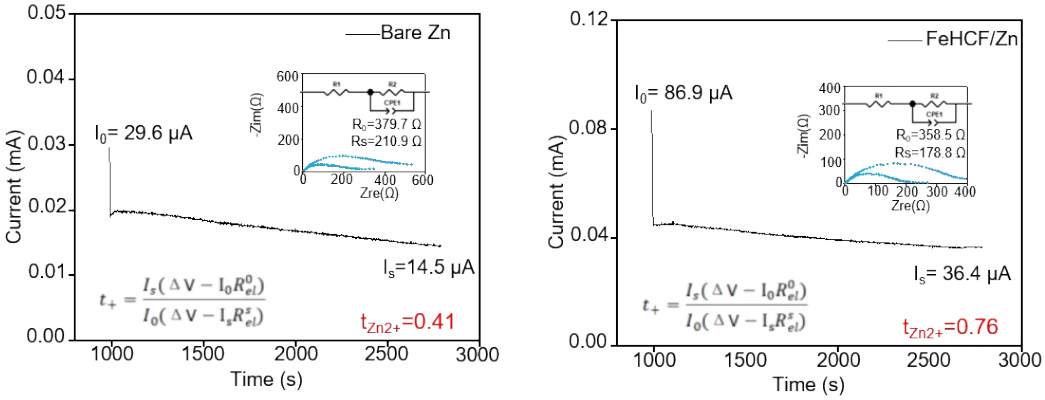

Figure S8. Current-time plots of symmetric Zn cells with bare Zn and FeHCF/Zn electrodes after polarization at a constant potential of 10 mV for 30 minutes, inset are the corresponding impedance spectra before and after polarization.

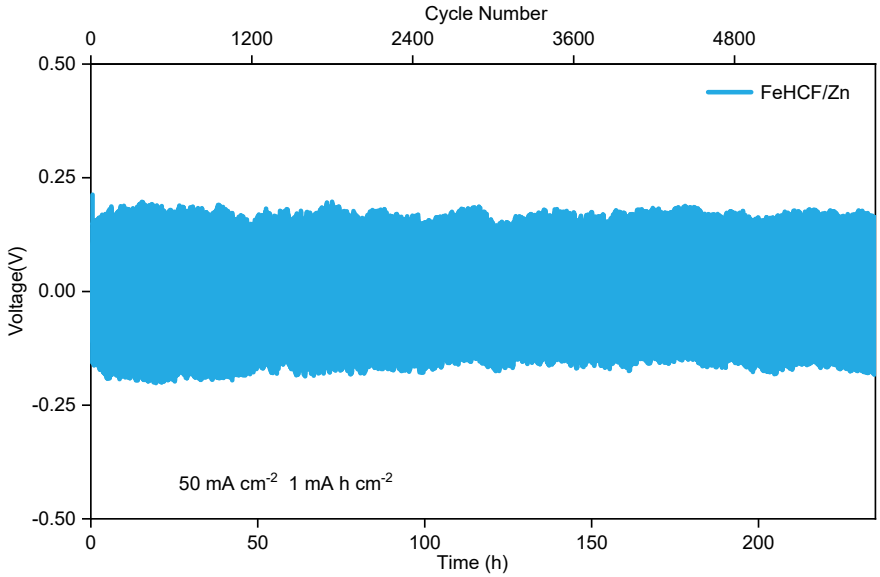

Figure S9. Cycling performance of FeHCF/Zn symmetric cells at 50 mA cm^{-2} and 1 mAh cm^{-2}.

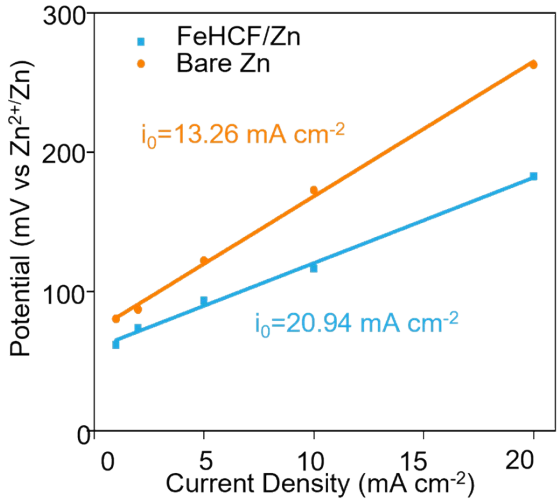

Figure S10. Exchange current densities.

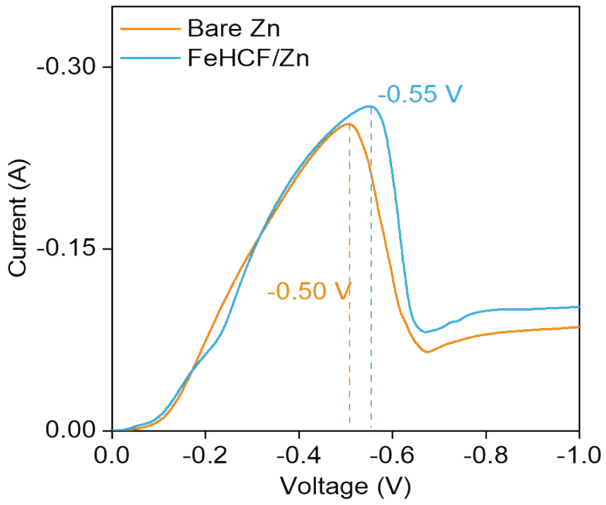

Figure S11. LSV curves of FeHCF/Zn and bare Zn at 50 mV s^{-1}.

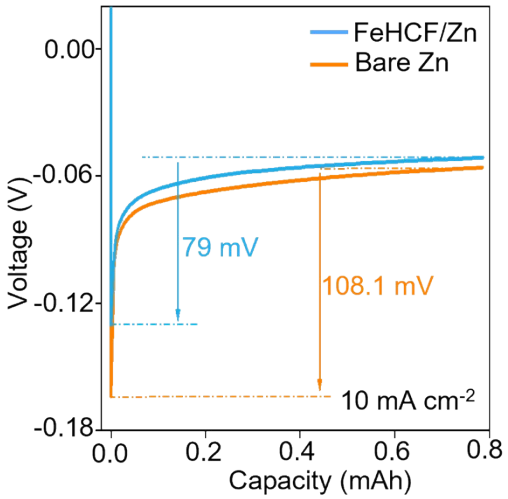

Figure S12. Zn nucleation overpotential for FeHCF/Zn and bare Zn at a current density of 10 mA cm^{-2}.

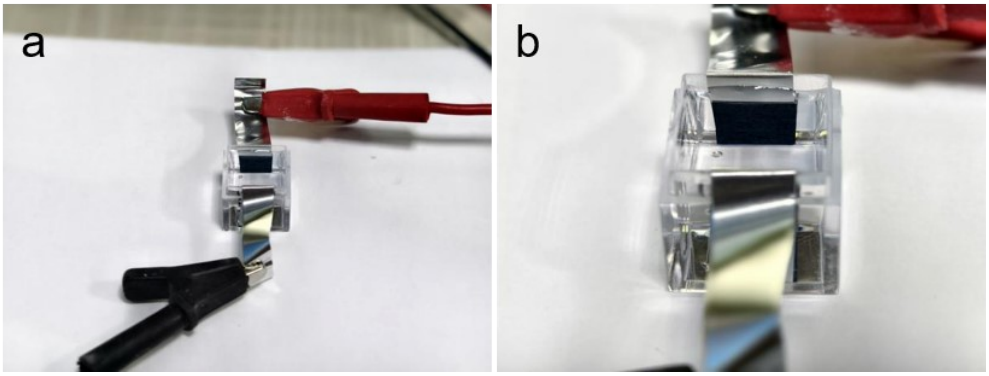

Figure S13. Photographs of the a) overall setup and b) close-up views of the experiment for Figure 3a.

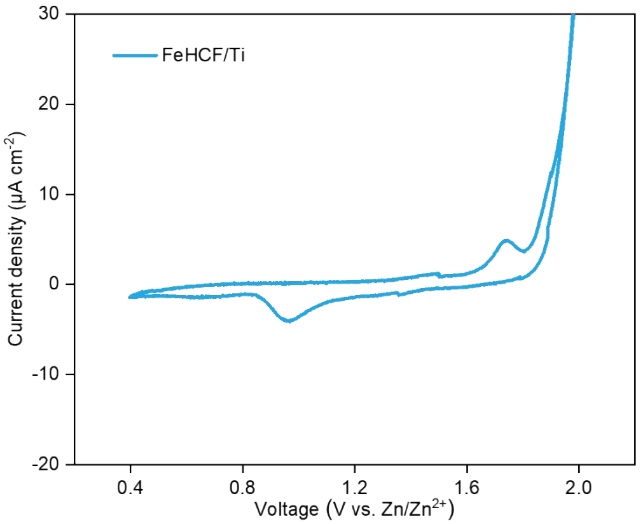

Figure S14. CV curve of the FeHCF/Ti||Zn cell.

Note 1. The theoretical capacity of FeHCF was calculated based on its molar mass and the number of electrons transferred during redox reactions. One mole of FeHCF has a molar mass of 268 g mol^{-1} and transfers 2 mol of electrons per mole during redox processes. Using Faraday's constant (F = 96,485 C mol^{-1}), the theoretical capacity can be calculated as:

Specific capacity=$F \times n/(3.6 \times M)$=96,485×2/(3.6×268)≈200mAh g^{-1}

Considering the mass of the FeHCF nanofilm: Mass = Density × Volume = 1.8 g cm^{-3} × 0.785 cm^2 × 16.9×10^{-7} cm ≈ 2.3×10^{-6} g

Therefore, the theoretical volumetric capacity is:

Volumetric capacity = Specific capacity × Mass / Volume=200 mAh g^{-1} × 2.3×10^{-6} g / (0.785 cm^2 × 16.9×10^{-7}cm) ≈ 346mAh cm^{-3}

The theoretical areal capacity is then:

Areal capacity = Volumetric capacity × Thickness = 346 mAh cm^{-3} × 16.9×10^{-7}cm ≈ 5.8×10^{-4} mAh cm^{-2}

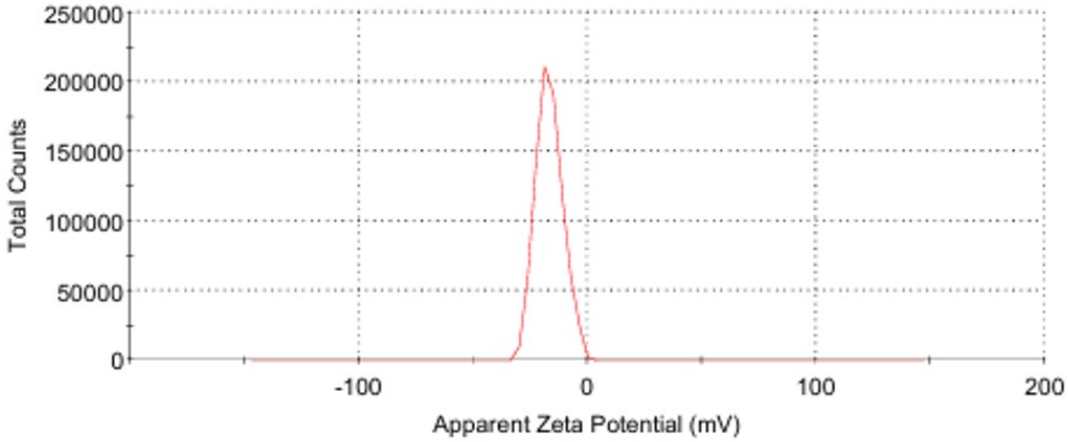

Figure S15. Zeta potential of the FeHCF nanomembrane after Zn plating.

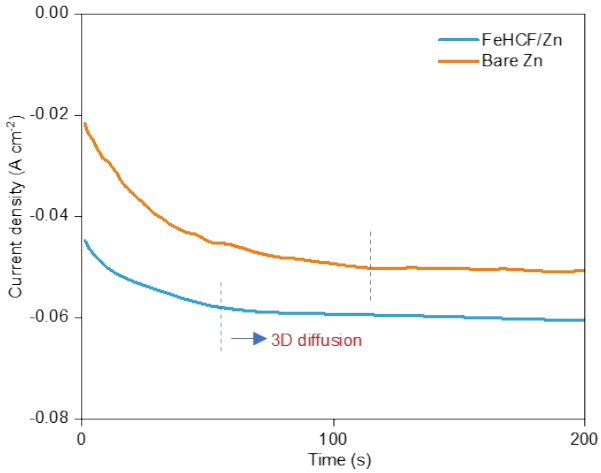

Figure S16. CA profiles of bare Zn and FeHCF/Zn at an overpotential of -150 mV.

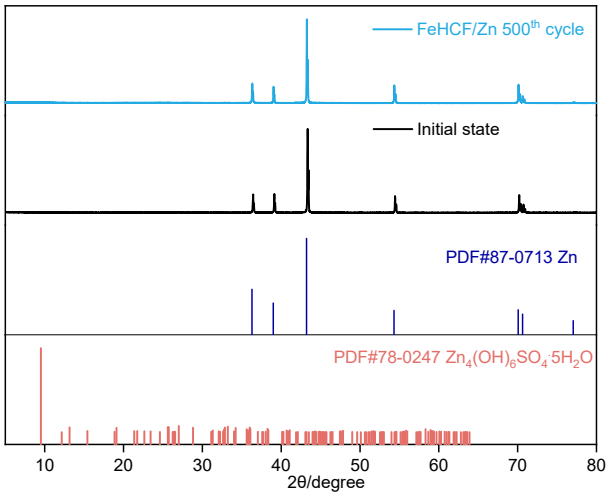

Figure S17. XRD patterns of FeHCF/Zn electrode after 500 cycles at 5 mA cm^{-2} and 1 mAh cm^{-2}.

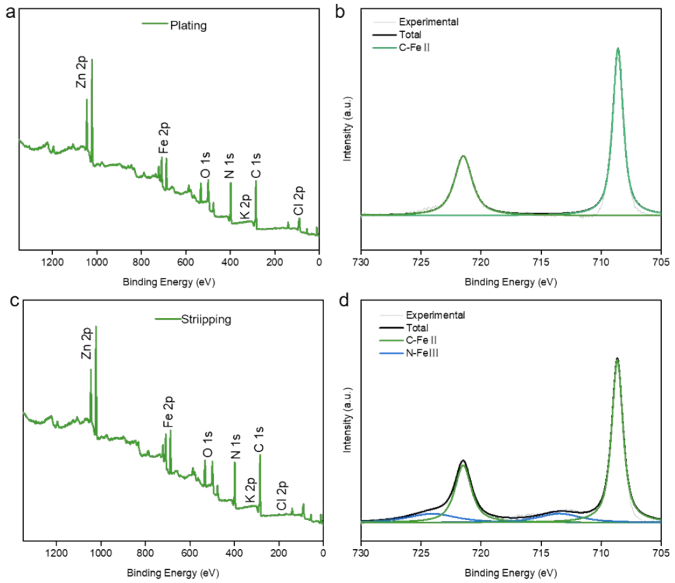

Figure S18. a) XPS survey scans and b) Fe 2p XPS of FeHCF/Zn electrode in symmetric cell at the plating side after 500 cycles at 10 mA cm^{-2}, 1 mAh cm^{-2}. c) XPS survey scans and d) Fe 2p XPS of FeHCF/Zn electrode in symmetric cell at the stripping side after 500 cycles at 10 mA cm^{-2}, 1 mAh cm^{-2}.

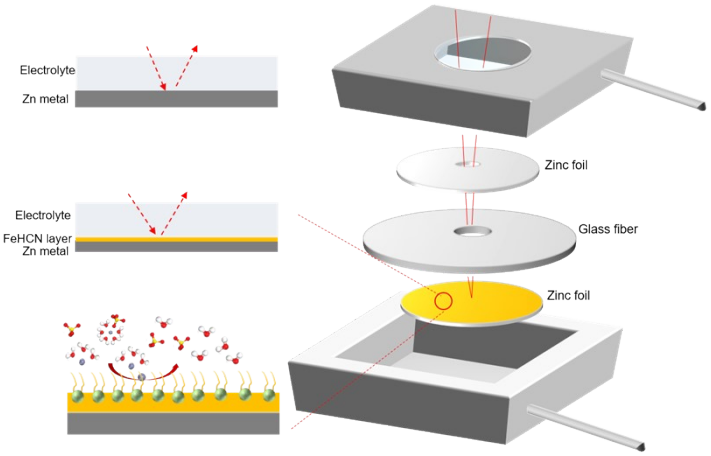

Figure S19. The cell setup for the *in-situ* Raman test.

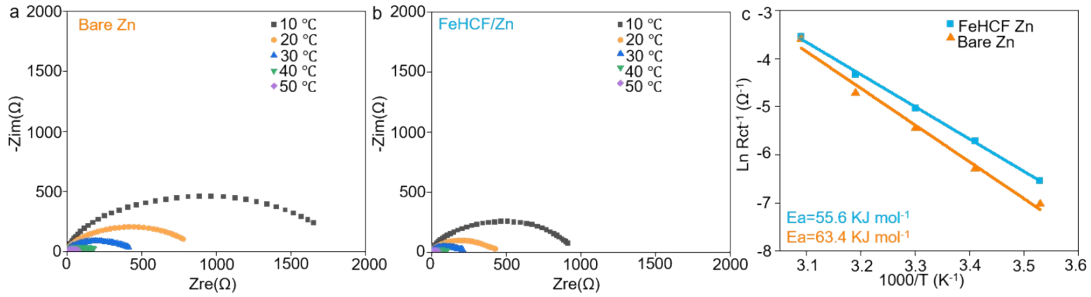

Figure S20. Nyquist plots of **a**) bare Zn and **b**) FeHCF/Zn symmetric cells at different temperatures. **c**, Desolvation activation energy (Ea) from Arrhenius curves.

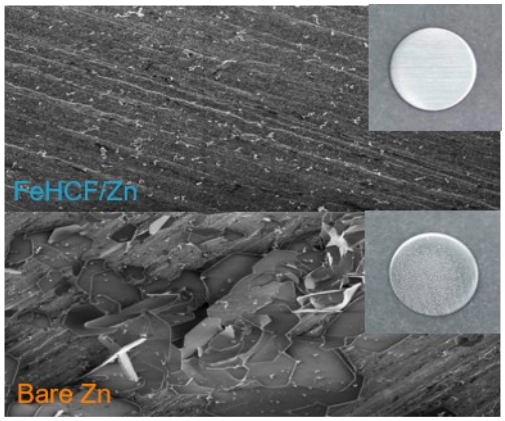

Figure S21. SEM images of FeHCF/Zn and bare Zn after immersed in the 2 M $ZnSO_4$ aqueous electrolyte for 3 day (inset: photograph of the immersed electrodes).

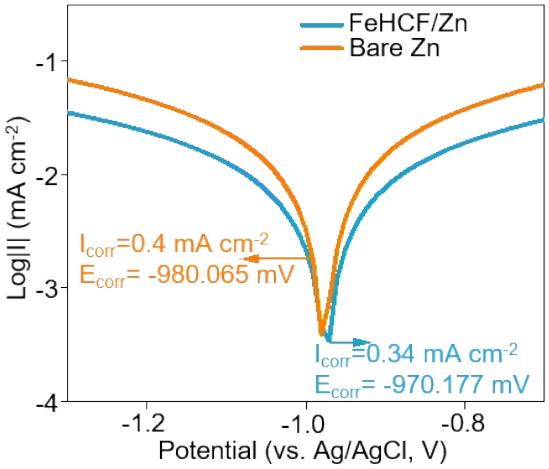

Figure S22. Linear polarization curves showing the corrosion on bare Zn and FeHCF/Zn electrodes.

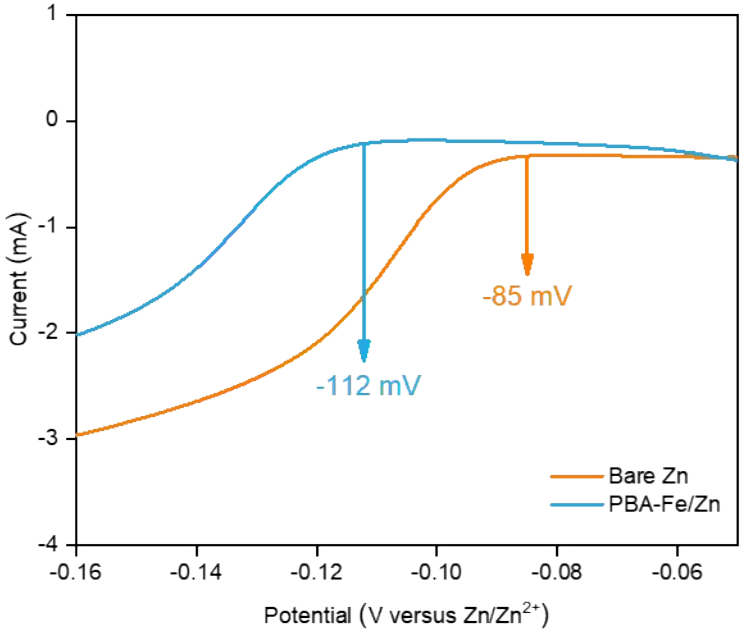

Figure S23. LSV curves of the cycled bare Zn and FeHCF/Zn electrodes in 1 M Na_2SO_4 electrolyte. The electrodes were cycled at 10 mA cm^{-2} and 1 mAh cm^{-2} for 10 cycles.

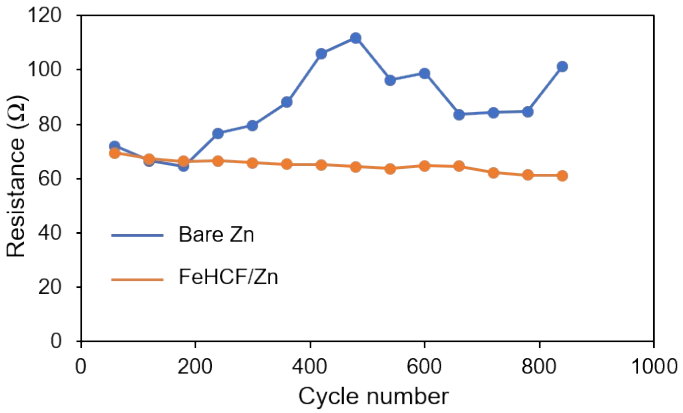

Figure S24. The fitted membrane resistance.

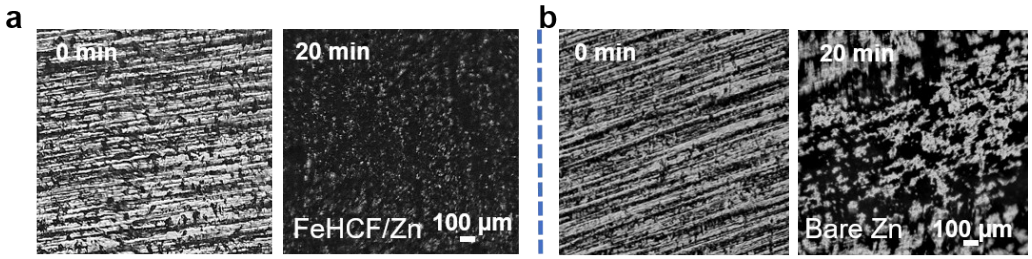

Figure S25. The optical images of **a**) FeHCF/Zn and **b**) bare Zn after plating for 20 min at 20 mA cm^{-2}.

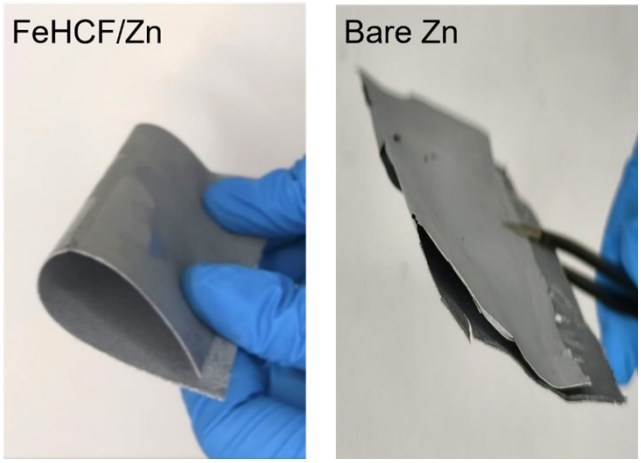

Figure S26. The folding of the free-standing deposited Zn metal foil.

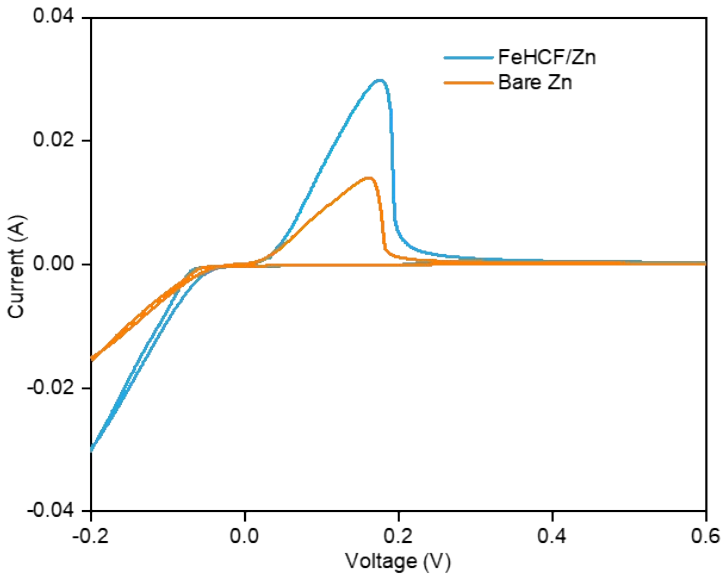

Figure S27. CV curves of FeHCF/Zn and bare Zn.

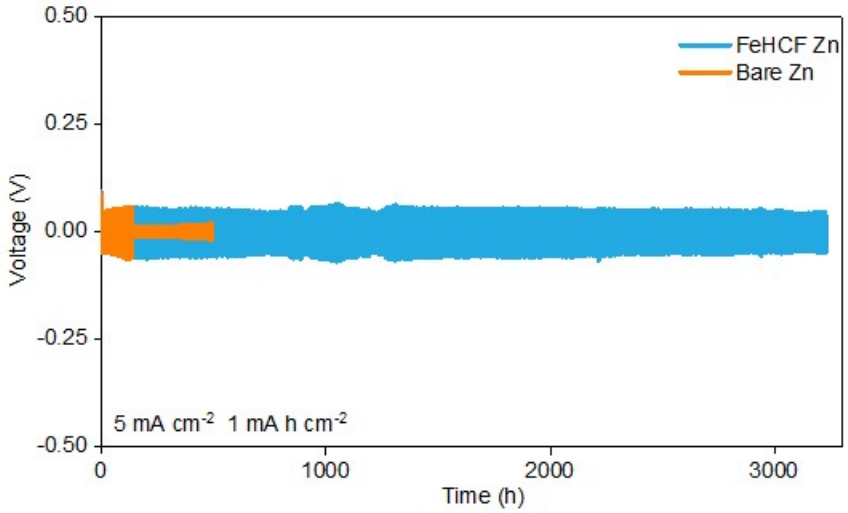

Figure S28. The cycling performance of the bare Zn and FeHCF/Zn symmetric cell at 5 mA cm^{-2}, 1 mAh cm^{-2}.

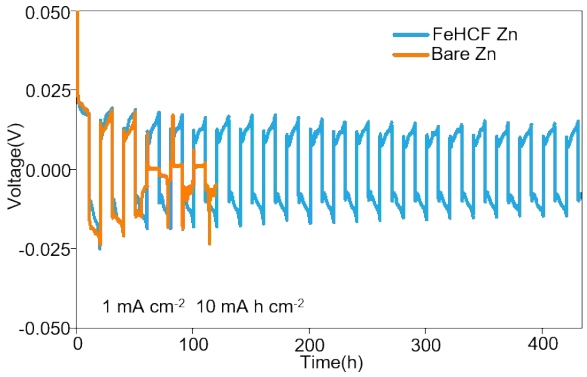

Figure S29. The cycling performance of the bare Zn and FeHCF/Zn symmetric cell at 1 mA cm^{-2}, 10 mAh cm^{-2}.

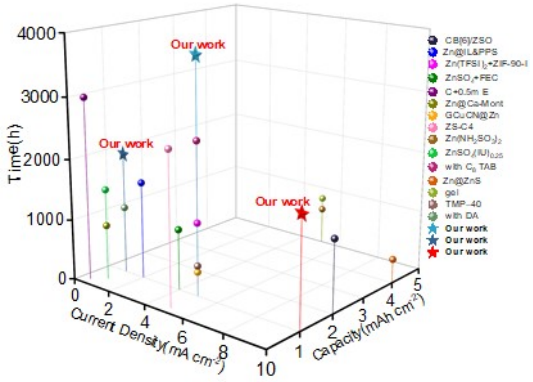

Figure S30. Comparison of cycling performances of FeHCF/Zn symmetric cell with reported data.

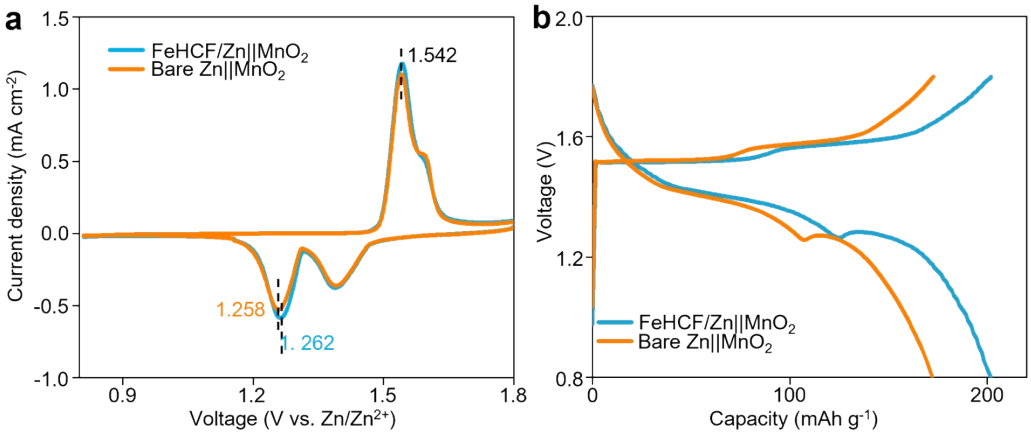

Figure S31. a, CV curves of Zn||MnO_2 full cells. **b**, Charge-discharge curves at 1 A g^{-1}.

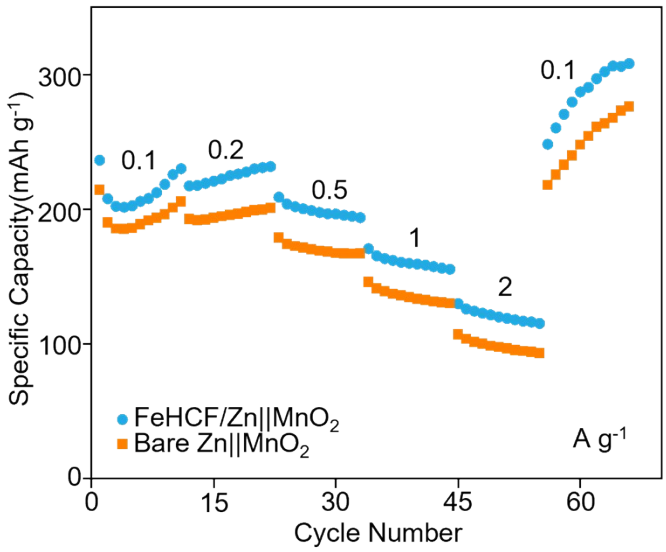

Figure S32. Rate capability of Zn||MnO_2 full cells from 0.1 to 2 A g^{-1}.

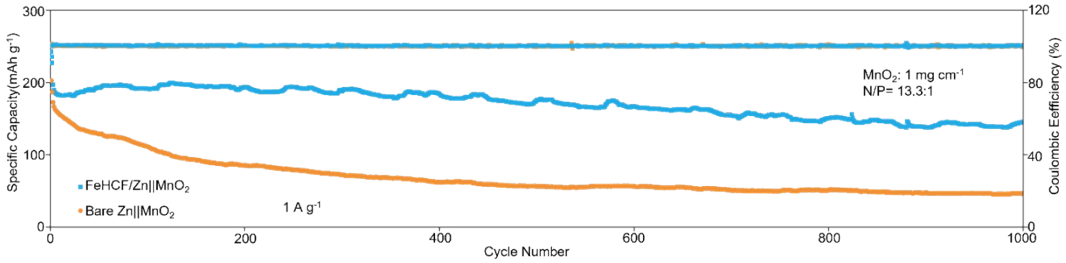

Figure S33. Cycling performance of Zn||MnO_2 full cells at an N/P ratio of 13.3:1.

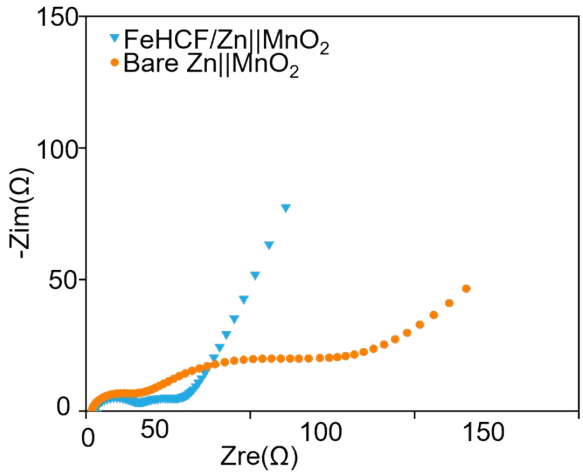

Figure S34. Impedance of Zn||MnO_2 full cells after 100 cycles at 1A/g.

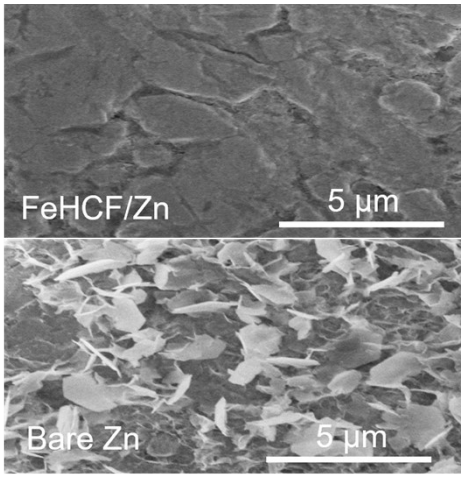

Figure S35. SEM images of the FeHCF/Zn and bare Zn electrodes in Zn||MnO_2 full cells after 100 cycles.

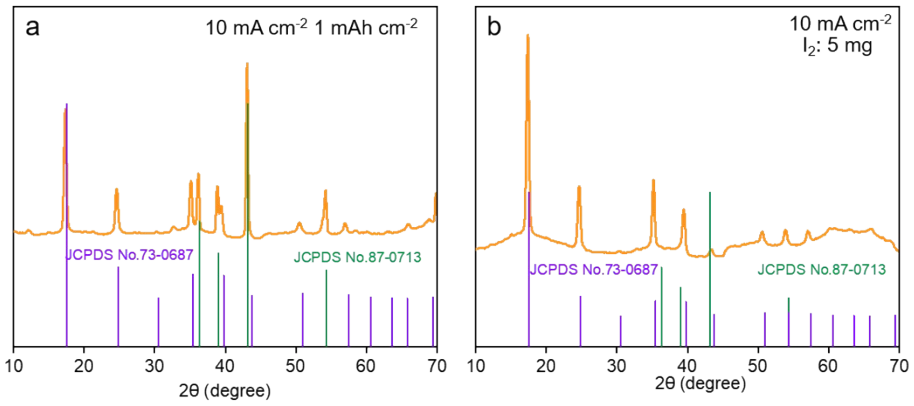

Figure S36. The XRD spectra of FeHCF protective layer after 500 cycles in a) Zn||Ti cell and b) Zn||I_2 cell.

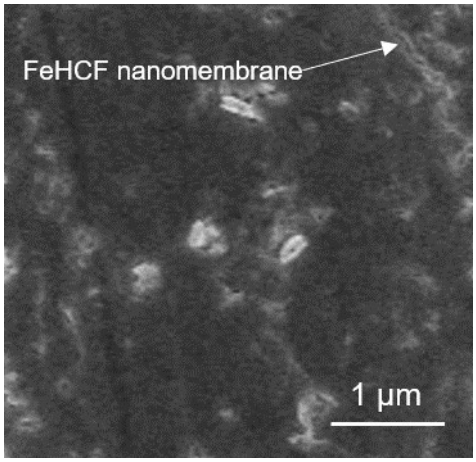

Figure S37. SEM image of the cycled FeHCF/Zn electrode.

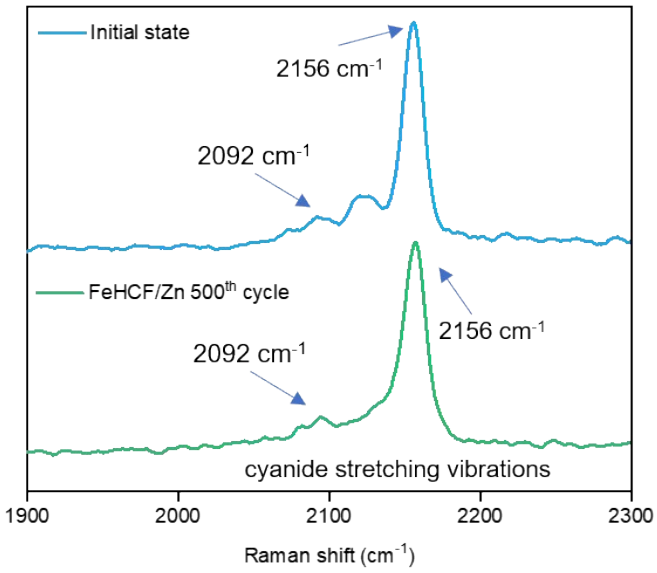

Figure S38. Raman spectra of the cycled FeHCF/Zn electrode.

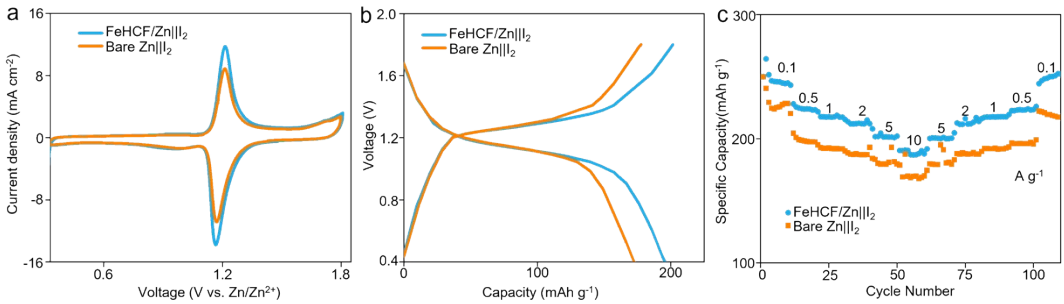

Figure S39. a, CV curves of Zn||I_2 full cells. b, Charge-discharge curves at 1 A g^{-1}. c, Rate capability of Zn||I_2 full cells.

Table S1. Summary of the performance of the asymmetric cells.

Composition	Current density (mA cm^{-2})	CE (%)	Cumulative capacity (mAh cm-2)	Refs
Coumarin	5	99.8	1600	Ref.1
CB[6]/ZSO	0.5	99.63	1000	Ref.2
$ZnSO_4$+FEC	4	99.1	500	Ref.3
C_8 TAB	1	99.8	1200	Ref.4
Glu/ZC/PAM	2	99.2	800	Ref.5
C+0.5 m E	0.5	99.8	500	Ref.6
Na-Zn WSEE	0.5	98.5	500	Ref.7
Zn@ZnS	5	98.9	2500	Ref.8
LHCE	1	99.7	200	Ref.9
ACG-SEI/Zn	1	99.8	1000	Ref.10
Zn@Ca-Mont	2	99.7	1000	Ref.11
ZIB/CCH	2	99.7	1000	Ref.12
$Zn(NH_2SO_3)_2$	1	99.65	1000	Ref.13
Zn@IL&PPS	1	99.5	100	Ref.14
ZS-C4	10	99.6	3000	Ref.15
DA	1	98.5	1000	Ref.16
FeHCF/Zn	5	99.8	10200	This work
FeHCF/Zn	10	99.94	10476	This work

Table S2. Summary of the performance of Zn symmetric cells.

Composition	Current density (mA cm^{-2})	Cumulative capacity (mAh cm-2)	Time (h)	Refs
CB[6]/ZSO	10	2	1200	Ref.2
Zn@IL&PPS	2	1	1600	Ref.14
$Zn(TFSI)_2$+ZIF-90-I	5	1	1200	Ref.17
$ZnSO_4$+FEC	4	1	1000	Ref.3
C+0.5 m E	0.5	0.25	3000	Ref.6
Zn@Ca-Mont	1	0.5	900	Ref.11
GCuCN@Zn	5	1	400	Ref.18
ZS-C4	5	0.25	2500	Ref.15
$Zn(NH2SO_3)_2$	5	5	600	Ref.13
$ZnSO_4(IU)_{0.25}$	1	0.5	1500	Ref.19
C_8 TAB	5	1	2500	Ref.4
Zn@ZnS	10	4	400	Ref.20
gle	5	5	800	Ref.21
TMP–40	5	1	500	Ref.22
DA	1	1	1100	Ref.16
FeHCF/Zn	5	1	3800	This work
FeHCF/Zn	10	1	1800	This work
FeHCF/Zn	1	1	2000	This work

Table S3. Summary of the performance of aqueous zinc ion batteries.

Composition	Current density (mA cm^{-2})	Cumulative capacity (mAh cm-2)	Refs
CB[6]/ZSO	10	2400	Ref.2
mPD@rGO/I_2	15	4069.5	Ref.23
NiSAs-HPC/I_2	30	12839	Ref.24
Zn//rGO–I_2	50	3140	Ref.25
Zn@TOP/Carra‖I_2	40	21195	Ref.26
Zn@COF-S-F	1.5	7500	Ref.27
2H8D	1	6000	Ref.28
Zn@Sn–ZnF2‖I_2	2.5	2080	Ref.29
Cu‖AC	50	7771.5	Ref.20
Zn(002)	5	9750	Ref.30
+2 wt% TDMA	1	9000	Ref.31
FeHCF/Zn	109	31319	This work

Table S4. Summary of the energy densities of aqueous zinc ion batteries.

Composition	Utilization Rate of Zn(%)	Energy Density(Wh kg^{-1})	Refs
ZIB/CCH	35%	81.6	Ref.12
AFZIB	100%	162	Ref.32
Cu‖Znxa-V_2O_5@Gr	100%	142	Ref.33
PAPE@Zn	66%	53	Ref.34
ZS-EAc	33.3%	122	Ref.35
ANF	37.8%	129.2	Ref.36
ZT-12/NS-20	20%	66.7	Ref.37
ZSO-YCl_3	32%	92.4	Ref.38
Zn‖NVO	95%	144.98	Ref.39
Zn/$Zn_{0.25}V_2O_5$	47.6%	47.5	Ref.40
Cu@G@Zn//PANI	42.5%	63.8	Ref.41
At-Sn@HCN	45%	140	Ref.42
Zn@Bi/Bi_2O_3‖MnO_2	15.8%	44.72	Ref.43
Bi@Zn	15%	138.6	Ref.44
FeHCF/Zn	100%	186	This work

Note 2. The energy density of the full cells was calculated using the equation:

$$E=\frac{Q_{cat}\times m_{cat}}{m_{cat}+m_{an}}\times V=\frac{159.09\ mAh/g\times 16\ mg}{0\ mg+16\ mg}\times 1.17\ V=186.135\ Wh/kg$$

Note 3. Water permeability were determined using the H-type diffusion cell. The cells were initially filled with 5.5 mL of a 2 M $ZnSO_4$ solution on the left compartment and 7 mL of deionized water on the right. The system was allowed to equilibrate for 2 hours.

The difference in water height in the receiving compartment after 2 hours of diffusion was measured. The mass of permeated water (m) was calculated from:

$m=\rho\times A'\times\Delta h$

where ρ=1 g/cm^3 is the water density, A' is the cross-sectional area of the receiving chamber (2.8938 cm^2), and Δh is the measured height difference.

The amount of water (n) was obtained by:

$n=mM_{H_2O}$

where M_{H_2O}=18 g/mol.

The permeability (P) was then calculated as:

$P=n/(A\times t\times p)$

where A (0.000078 m^2) is the membrane area, t (2 h) is the diffusion time, and p is the osmotic pressure at room temperature

The osmotic pressure was calculated as:

p = n * Φ * c * R * T

where n is the number of ions produced when the solute undergoes dissociation, Φ is Osmotic coefficient of the $ZnSO_4$, c is molar concentration of the solution, R is the universal gas constant, T is the temperature. The calculated p value is 5,751,000Pa.

For the FeHCF/PP membrane:

Δh=0.16 cm

m = 1 g/cm^3 × 2.8938 cm^2 × 0.16 cm= 0.463008 g

n = 0.463008 g / 18 g/mol=0.025723 mol

P=0.025723mol/(0.000078 m^2×2 h×5,751,000 Pa)=0.000028 mol m^{-2}h^{-1}Pa^{-1}

For the bare PP membrane:

Based on Figure 2b, the slope of the tangent was calculated as 0.017 cm min^{-1}, after 2 hours:

Δh=0.017 cm min^{-1} *120 min

m = 1 g/cm^3 × 2.8938 cm^2 × 2.04 cm = 5.9033 g

n = 5.9033 g / 18 g/mol = 0.32796 mol

P = 0.32796 mol / (0.000078 m^2 × 2 h × 5,751,000 Pa)=0.000365 mol m^{-2}h^{-1}Pa^{-1}

References

[1] Z. Li, Z. Shu, Z. Shen, Y. Liu, Y. Ji, L. Luo, R. Li, Y. Cai, H. Ian, J. Xie, G. Hong. Dissolution Mechanism for Dendrite-Free Aqueous Zinc-Ions Batteries. *Advanced Energy Materials* **2024**, 14 (22): 2400572.
[2] X. Yang, Y. Zhao, S. Lv, L. Zhong, C. Yue, S. Zhan, L. Zhao, C. Wang, X. Li, X. Liu, Z. Tang, C. Zhang, C. Zhi, H. Lv. Anion-Promoted CB[6] Macromolecule Dissolution for Stable Zn-Ion Batteries. *Energy & Environmental Science* **2024**, 17 (13): 4758-4769.
[3] D. Xie, Y. Sang, D.H. Wang, W.Y. Diao, F.Y. Tao, C. Liu, J.W. Wang, H.Z. Sun, J.P. Zhang, X.L. Wu. ZnF_2-Riched Inorganic/Organic Hybrid SEI: In Situ-Chemical Construction and Performance-Improving Mechanism for Aqueous Zinc-Ion Batteries. *Angewandte Chemie International Edition* **2023**, 62 (7): e202216934.
[4] D. Tang, X. Zhang, D. Han, C. Cui, Z. Han, L. Wang, Z. Li, B. Zhang, Y. Liu, Z. Weng, Q.H. Yang. Switching Hydrophobic Interface with Ionic Valves for Reversible Zinc Batteries. *Advanced Materials* **2024**, 36 (33): e2406071.
[5] Y. Wang, L.e. Mo, X. Zhang, Y. Ren, T. Wei, Y. He, Y. Huang, H. Zhang, P. Tan, Z. Li, J. Zhou, L. Hu. Regulating Water Activity for All-Climate Aqueous Zinc-Ion Batteries. *Advanced Energy Materials* **2024**, 14 (33): 2402041.
[6] J. Ge, Y. Zhang, Z. Xie, H. Xie, W. Chen, B. Lu. Tailored Znf2/Zns-Rich Interphase for Reversible Aqueous Zn Batteries. *Nano Research* **2023**, 16 (4): 4996-5005.
[7] Y. Yang, G. Qu, H. Wei, Z. Wei, C. Liu, Y. Lin, X. Li, C. Han, C. Zhi, H. Li. Weakly Solvating Effect Spawning Reliable Interfacial Chemistry for Aqueous Zn/Na Hybrid Batteries. *Advanced Energy Materials* **2023**, 13 (12): 2203729.
[8] Y. Chen, Z. Deng, Y. Sun, Y. Li, H. Zhang, G. Li, H. Zeng, X. Wang. Ultrathin Zincophilic Interphase Regulated Electric Double Layer Enabling Highly Stable Aqueous Zinc-Ion Batteries. *Nano-Micro Letters* **2024**, 16 (1): 96.
[9] H. Li, Z. Chen, L. Zheng, J. Wang, H. Adenusi, S. Passerini, H. Zhang. Electrolyte Strategies Facilitating Anion-Derived Solid-Electrolyte Interphases for Aqueous Zinc-Metal Batteries. *Small Methods* **2024**, 8 (6): e2300554.
[10] M. Zhao, J. Rong, F. Huo, Y. Lv, B. Yue, Y. Xiao, Y. Chen, G. Hou, J. Qiu, S. Chen. Semi-Immobilized Ionic Liquid Regulator with Fast Kinetics toward Highly Stable Zinc Anode under -35 to 60 Degrees C. *Advanced Materials* **2022**, 34 (32): e2203153.
[11] L. Hong, X. Wu, C. Ma, W. Huang, Y. Zhou, K.-X. Wang, J.-S. Chen. Boosting the Zn-Ion Transfer Kinetics to Stabilize the Zn Metal Interface for High-Performance Rechargeable Zn-Ion Batteries. *Journal of Materials Chemistry A.* **2021**, 9 (31): 16814-16823.
[12] J.L. Yang, T. Xiao, T. Xiao, J. Li, Z. Yu, K. Liu, P. Yang, H.J. Fan. Cation-Conduction Dominated Hydrogels for Durable Zinc-Iodine Batteries. *Advanced Materials* **2024**, 36 (21): e2313610.
[13] X. Xu, H. Su, J. Zhang, Y. Zhong, Y. Xu, Z. Qiu, H.B. Wu, X. Wang, C. Gu, J. Tu. Sulfamate-Derived Solid Electrolyte Interphase for Reversible Aqueous Zinc Battery. *ACS Energy Letters* **2022**, 7 (12): 4459-4468.
[14] G. Gao, X. Huo, B. Li, J. Bi, Z. Zhou, Z. Du, W. Ai, W. Huang. Customizing the Water-Scarce, Zinc Ion-Rich Helmholtz Plane of a Zinc Anode for Ah-Scale Zn Metal Batteries. *Energy & Environmental Science* **2024**, 17 (20): 7850-7859.

[15] Z. Hu, F. Zhang, F. Wu, H. Wang, A. Zhou, Y. Chen, T. Xue, R. Chen, L. Li. Screening Metal Cation Additives Driven by Differential Capacitance for Zn Batteries. *Energy & Environmental Science* **2024**, 17 (13): 4794-4802.
[16] X. Zeng, K. Xie, S. Liu, S. Zhang, J. Hao, J. Liu, W.K. Pang, J. Liu, P. Rao, Q. Wang, J. Mao, Z. Guo. Bio-Inspired Design of Anin Situmultifunctional Polymeric Solid–Electrolyte Interphase for Zn Metal Anode Cycling at 30 mA cm^{-2} and 30 mAh cm^{-2}. *Energy & Environmental Science* **2021**, 14 (11): 5947-5957.
[17] Y. Zhao, H. Hong, L. Zhong, J. Zhu, Y. Hou, S. Wang, H. Lv, P. liang, Y. Guo, D. Wang, P. Li, Y. Wang, Q. Li, S.C. Cao, H. Li, C. Zhi. Zn-Rejuvenated and Sei-Regulated Additive in Zinc Metal Battery Via the Iodine Post-Functionalized Zeolitic Imidazolate Framework-90. *Advanced Energy Materials* **2023**, 13 (28): 2300627.
[18] W. Zhang, Q. Yao, C. Wang, R. Feng, N. Chen, J. Zhu, Z. Li. Taming Zn Electrochemistry with Carbon Nitride: Atomically Gradient Interphase for Highly Reversible Aqueous Zn Batteries. *Advanced Functional Materials* **2023**, 34 (5): 2303590.
[19] X. Wang, Y. Ying, X. Li, S. Chen, G. Gao, H. Huang, L. Ma. Preferred Planar Crystal Growth and Uniform Solid Electrolyte Interfaces Enabled by Anion Receptors for Stable Aqueous Zn Batteries. *Energy & Environmental Science* **2023**, 16 (10): 4572-4583.
[20] W. Shi, Z. Song, W. Zhang, S. Lian, F. Huang, Q. An, Q. Li. Identifying Iodide-Ion Regulation of Early-Stage Zinc Nucleation and Growth for High-Rate Anode-Free Zinc Metal Batteries. *Energy & Environmental Science* **2024**, 17 (19): 7372-7381.
[21] D. Yuan, X. Li, H. Yao, Y. Li, X. Zhu, J. Zhao, H. Zhang, Y. Zhang, E.T.J. Jie, Y. Cai, M. Srinivasan. A Liquid Crystal Ionomer-Type Electrolyte toward Ordering-Induced Regulation for Highly Reversible Zinc Ion Battery. *Advanced Science* **2023**, 10 (8): e2206469.
[22] W. Wang, S. Chen, X. Liao, R. Huang, F. Wang, J. Chen, Y. Wang, F. Wang, H. Wang. Regulating Interfacial Reaction through Electrolyte Chemistry Enables Gradient Interphase for Low-Temperature Zinc Metal Batteries. *Nature Communication* **2023**, 14 (1): 5443.
[23] F. Wei, T. Zhang, H. Xu, Y. Peng, H. Guo, Y. Wang, S. Guan, J. Fu, C. Jing, J. Cheng, S. Liu. 2D Mesoporous Naphthalene-Based Conductive Heteroarchitectures toward Long-Life, High-Capacity Zinc-Iodine Batteries. *Advanced Functional Materials* **2023**, 34 (4): 2310693.
[24] L. Ma, G. Zhu, Z. Wang, A. Zhu, K. Wu, B. Peng, J. Xu, D. Wang, Z. Jin. Long-Lasting Zinc-Iodine Batteries with Ultrahigh Areal Capacity and Boosted Rate Capability Enabled by Nickel Single-Atom Electrocatalysts. *Nano Letters* **2023**, 23 (11): 5272-5280.
[25] Y. Ji, J. Xie, Z. Shen, Y. Liu, Z. Wen, L. Luo, G. Hong. Advanced Zinc–Iodine Batteries with Ultrahigh Capacity and Superior Rate Performance Based on Reduced Graphene Oxide and Water-in-Salt Electrolyte. *Advanced Functional Materials* **2023**, 33 (10): 2210043.
[26] Y. Xu, M. Zhang, R. Tang, S. Li, C. Sun, Z. Lv, W. Yang, Z. Wen, C.C. Li, X. Li, Y. Yang. A Plant Root Cell-Inspired Interphase Layer for Practical Aqueous Zinc–Iodine

Batteries with Super-High Areal Capacity and Long Lifespan. *Energy & Environmental Science* **2024**, 17 (18): 6656-6665.
[27] B. Li, P. Ruan, X. Xu, Z. He, X. Zhu, L. Pan, Z. Peng, Y. Liu, P. Zhou, B. Lu, L. Dai, J. Zhou. Covalent Organic Framework with 3d Ordered Channel and Multi-Functional Groups Endows Zn Anode with Superior Stability. *Nano-Micro Letters* **2024**, 16 (1): 76.
[28] D. Li, Y. Zhong, X. Xu, D. Zhou, Y. Tang, L. Wang, S. Liang, B. Lu, Y. Liu, J. Zhou. Reinforcing the Symmetry of Stripping/Plating Behavior Via in Situ Interface Construction for Long-Lasting Zinc Metal Batteries. *Energy & Environmental Science* **2024**, 17 (22): 8855-8865.
[29] G. Wang, Q. Yao, J. Dong, W. Ge, N. Wang, Z. Bai, J. Yang, S. Dou. In Situ Construction of Multifunctional Surface Coatings on Zinc Metal for Advanced Aqueous Zinc–Iodine Batteries. *Advanced Energy Materials* **2023**, 14 (5): 2303221.
[30] Y. Li, X. Ma, X. Zhang, F. Zhang, Q. Wang, Q. Guo, J. Liu, Y. Wang, J. Huang, Y. Xia. High Zn(002)-Preferential Orientation Enabled by a Proton Additive for Dendrite-Free Zinc Anodes. *Energy & Environmental Science* **2024**, 17 (23): 9205-9214.
[31] G.R. Pastel, T.P. Pollard, Q. Liu, S. Lavan, Q. Zhu, R. Jiang, L. Ma, J. Connell, O. Borodin, M.A. Schroeder, Z. Zhang, K. Xu. Designing Interphases for Highly Reversible Aqueous Zinc Batteries. *Joule* **2024**, 8 (4): 1050-1062.
[32] Y. Zhang, L. Wang, Q. Li, B. Hu, J. Kang, Y. Meng, Z. Zhao, H. Lu. Iodine Promoted Ultralow Zn Nucleation Overpotential and Zn-Rich Cathode for Low-Cost, Fast-Production and High-Energy Density Anode-Free Zn-Iodine Batteries. *Nano-Micro Letters* **2022**, 14 (1): 208.
[33] H.-I. Kim, K.M. Lee, W.-Y. Kim, S.H. Kweon, X. Wang, S. Zheng, S.-H. Kim, J.H. Ha, S.J. Kang, Z.-S. Wu, S.K. Kwak, S.-Y. Lee. Restructuring of Aqueous Electrolytes Using a Soft-Acidic/Hard-Basic Zwitterion for Low-Temperature Anode-Free Zn Batteries. *Energy & Environmental Science* **2024**, 17 (5): 1961-1974.
[34] J. Feng, X. Li, Y. Ouyang, H. Zhao, N. Li, K. Xi, J. Liang, S. Ding. Regulating Zn^{2+} Migration-Diffusion Behavior by Spontaneous Cascade Optimization Strategy for Long-Life and Low N/P Ratio Zinc Ion Batteries. *Angewandte Chemie International Edition* **2024**, 63 (41): e202407194.
[35] T. Xiao, J. L. Yang, B. Zhang, J. Wu, J. Li, W. Mai, H. J. Fan. All-Round Ionic Liquids for Shuttle-Free Zinc-Iodine Battery. *Angew Chem Int Ed* **2024**, 63 (8): e202318470.
[36] L. Yang, Y.J. Zhu, H.P. Yu, Z.Y. Wang, L. Cheng, D.D. Li, J. Tao, G. He, H. Li. A Five Micron Thick Aramid Nanofiber Separator Enables Highly Reversible Zn Anode for Energy-Dense Aqueous Zinc-Ion Batteries. *Advanced Energy Materials* **2024**, 14 (39): 2401858.
[37] R. Wang, Z. Liu, J. Wan, X. Zhang, D. Xu, W. Pan, L. Zhang, H. Li, C. Zhang, Q. Zhang. Eutectic Network Synergy Interface Modification Strategy to Realize High-Performance Zn-I_2 Batteries. *Advanced Energy Materials* **2024**, 14 (44): 2402900.
[38] Y. Chen, S. Zhou, J. Li, J. Kang, S. Lin, C. Han, H. Duan, S. liang, A. Pan. Non-Expendable Regulator Enables Durable and Deep Cycling Aqueous Zinc Batteries. *Advanced Energy Materials* **2024**, 14 (25): 2400398.
[39] Z. Xu, H. Li, Y. Liu, K. Wang, H. Wang, M. Ge, J. Xie, J. Li, Z. Wen, H. Pan, S. Qu, J. Liu, Y. Zhang, Y. Tang, S. Chen. Durable Modulation of Zn(002) Plane Deposition

Via Reproducible Zincophilic Carbon Quantum Dots Towards Low N/P Ratio Zinc-Ion Batteries. *Materials Horizons* **2023**, 10 (9): 3680-3693.
[40] Y. Pan, Z. Zuo, Y. Jiao, P. Wu. Constructing Lysozyme Protective Layer Via Conformational Transition for Aqueous Zn Batteries. *Advanced Materials* **2024**, 36 (29): e2314144.
[41] M. Xi, Z. Liu, W. Wang, Z. Qi, R. Sheng, J. Ding, Y. Huang, Z. Guo. Shear-Flow Induced Alignment of Graphene Enables the Closest Packing Crystallography of the (002) Textured Zinc Metal Anode with High Reversibility. *Energy & Environmental Science* **2024**, 17 (9): 3168-3178.
[42] X. Zhang, C. Qu, X. Zhang, X. Peng, Y. Qiu, Y. Su, J. Zeng, Z. Liu, X. Liu, W. Qi, H. Wang, F. Xu. Atomic Sn Encapsulation with Visualizing Mitigated Active Zinc Loss toward Anode-Lean Zinc Metal Battery. *Advanced Energy Materials* **2024**, 14 (30): 2401139.
[43] X. Tian, Q. Zhao, M. Zhou, X. Huang, Y. Sun, X. Duan, L. Zhang, H. Li, D. Su, B. Jia, T. Ma. Synergy of Dendrites-Impeded Atomic Clusters Dissociation and Side Reactions Suppressed Inert Interface Protection for Ultrastable Zn Anode. *Advanced Materials* **2024**, 36 (19): e2400237.
[44] H. Chen, W. Zhang, S. Yi, Z. Su, Z. Zhao, Y. Zhang, B. Niu, D. Long. Zinc Iso-Plating/Stripping: Toward a Practical Zn Powder Anode with Ultra-Long Life over 5600 H. *Energy & Environmental Science* **2024**, 17 (9): 3146-3156.